Eddy Influences on the Strength of the Hadley Circulation: Dynamic and Thermodynamic Perspectives

MARTIN S. SINGH,[a] ZHIMING KUANG, AND YANG TIAN

Department of Earth and Planetary Sciences, Harvard University, Cambridge, Massachusetts

(Manuscript received 11 August 2016, in final form 28 October 2016)

ABSTRACT

The strength of the equinoctial Hadley circulation (HC) is investigated in idealized simulations conducted on an equatorial beta plane in which the zonal width of the domain is varied to either permit or suppress large-scale eddies. The presence of such eddies is found to amplify the HC by a factor of 2–3 in simulations with slab-ocean boundary conditions or with a simple representation of ocean heat transport. Additional simulations in which the eddy forcing is prescribed externally indicate that this amplification is primarily associated with large-scale eddy momentum fluxes rather than large-scale eddy heat fluxes. These results contrast with results from simulations with fixed distributions of sea surface temperature (SST), in which the HC strength has been found to be relatively insensitive to large-scale eddy momentum fluxes.

In both the interactive- and fixed-SST cases, the influence of nonlinear momentum advection by the mean flow complicates efforts to use the angular-momentum budget to constrain the HC strength. However, a strong relationship is found between the HC strength and a measure of the meridional gradient of boundary layer entropy, indicating a possible thermodynamic control on the HC strength. In simulations with interactive SSTs, meridional eddy momentum fluxes affect the boundary layer entropy by inducing a low-level frictional flow that reduces the ability of the HC to transport heat poleward. This allows for the maintenance of a large meridional entropy gradient in the presence of a strong HC. The results highlight the potential utility of a thermodynamic perspective for understanding the HC in flow regimes for which dynamical constraints may be difficult to apply.

1. Introduction

The potential importance of midlatitude baroclinic eddies in determining the characteristics of Earth's Hadley circulation (HC) has long been recognized (e.g., Kuo 1956; Dickinson 1971; Pfeffer 1981). Previous authors have attempted to quantify the effect of such large-scale eddies on the tropical overturning circulation by comparing general circulation model (GCM) simulations run in axisymmetric and three-dimensional configurations (e.g., Williams 1988a,b). For example, in idealized simulations forced by Newtonian relaxation of temperatures to an equilibrium distribution, the equinoctial HC has been found to be stronger by a factor of 2 or more in the presence of eddies compared to in the axisymmetric case (Becker et al. 1997; Kim and Lee 2001; Walker and Schneider 2005). On the other hand, Satoh et al. (1995) and Singh and Kuang (2016, hereafter SK16) have found that, in simulations in which the distribution of sea surface temperature (SST) is fixed, the equinoctial HC achieves a similar strength with or without the influence of large-scale eddies. These contrasting results motivate us to extend SK16 to the case of energetically closed boundary conditions and to explore the role of large-scale eddies in determining the strength of the tropical overturning circulation in this more general setting.

One approach to understanding the influence of large-scale eddies on the HC is to consider the atmospheric budget of angular momentum (e.g., Becker et al. 1997). Under steady-state conditions, this budget requires a balance between the eddy momentum flux divergence and the mean-flow advection of angular momentum in the subtropical upper troposphere. In the linear limit, in which the meridional gradient of angular momentum is dominated by its planetary component, this mean-flow advection may be directly related to the intensity of the meridional flow in the upper branch of the HC. Indeed, Walker and Schneider (2006) showed that the strength of the equinoctial HC varies roughly in proportion to a measure of the subtropical eddy momentum flux

[a] Current affiliation: School of Earth, Atmosphere and Environment, Monash University, Clayton, Victoria, Australia.

Corresponding author e-mail: Martin S. Singh, martin.singh@monash.edu

DOI: 10.1175/JAS-D-16-0238.1

divergence in a set of idealized GCM simulations run over a wide range of parameters. A number of more recent studies have adopted this dynamic perspective to analyze the influence of eddies on the HC in both realistic (Caballero 2007, 2008; Bordoni and Schneider 2008) and idealized (Bordoni and Schneider 2010; Schneider and Bordoni 2008) configurations.

If the flow is outside the linear regime, as it is in the observed cross-equatorial winter HC (Bordoni and Schneider 2008), nonlinear advection of angular momentum by the mean circulation is nonnegligible, and the relationship between the eddy momentum fluxes and the HC strength may not be straightforward. Under these conditions, the predictive value of the dynamic perspective is reduced. Moreover, the dynamic perspective is not well suited to exploring the reasons for the insensitivity of the HC strength to large-scale eddy fluxes in the fixed-SST simulations of SK16 and Satoh et al. (1995). Rather, the results of these studies point to the possible relevance of theories of the HC based on axisymmetric models (e.g., Schneider 1977; Held and Hou 1980; Lindzen and Hou 1988; Plumb and Hou 1992; Satoh 1994; Fang and Tung 1996; Caballero et al. 2008), in which a thermodynamic constraint is used to determine the HC strength. In particular, Emanuel (1995) used the assumption of convective quasi equilibrium (Emanuel et al. 1994) to argue that, in the limit of vanishing absolute vorticity at the tropopause, the strength of the tropical overturning circulation may be related to a measure of the horizontal gradient in boundary layer entropy. Within this framework, eddies may influence the strength of the mean circulation only to the extent that they affect the boundary layer entropy distribution, and their influence is limited when the boundary layer entropy is constrained by specifying the SST.

Since the meridional heat (energy) transport in the atmosphere strongly influences the SST and boundary layer entropy, the thermodynamic perspective embodied in Emanuel (1995) also highlights the potential importance of meridional eddy heat fluxes in determining the HC strength. Indeed, Trenberth and Stepaniak (2003) used an analysis of the observed energy budget to argue that large-scale eddy heat fluxes may be a fundamental driver of Earth's HC. On the other hand, Schneider (1984) found that removing the effect of eddy heat fluxes resulted in only a modest reduction in the subtropical temperature gradient and HC strength in simulations in which the convective heating and eddy momentum fluxes were specified.

In this study, we investigate the relative roles of large-scale eddy momentum fluxes and large-scale eddy heat fluxes in determining the strength of the HC in simulations with an explicit representation of moist convection, and we explore the conditions under which the dynamic and thermodynamic perspectives outlined above may be useful for understanding these eddy–mean flow interactions. Following SK16, we conduct idealized simulations of an equinoctial HC in a moist atmosphere using an equatorial beta-plane model. Simulations are conducted in two configurations: a wide-domain configuration, in which the model domain is planetary scale in both latitude and longitude and large-scale eddies are permitted, and a narrow-domain configuration, in which the model domain is planetary scale in latitude but occupies only a few degrees of longitude and large-scale eddies do not form. Extending the fixed-SST simulations of SK16, we consider both slab-ocean simulations and simulations with a simple parameterization of low-latitude ocean heat transport following that of Levine and Schneider (2011).

Comparisons of the results from the wide- and narrow-domain configurations reveal a substantial amplification of the HC owing to the presence of large-scale eddies. Furthermore, using simulations in which the effects of large-scale meridional eddy fluxes are externally imposed, this amplification of the HC is attributed primarily to eddy fluxes of momentum rather than eddy fluxes of heat (cf. Schneider 1984). The relationship between these results and previous studies using fixed-SST boundary conditions is discussed, and it is argued that considerable insight may be gained by adopting a thermodynamic perspective of the HC, particularly when the flow regime is nonlinear and dynamical constraints may be difficult to apply.

The rest of this paper is organized as follows: We first describe the model configuration and simulations (section 2), and we present a comparison of results from the wide-domain and narrow-domain configurations (section 3). Next, we consider simulations in which the effects of large-scale meridional eddy fluxes of heat and momentum are imposed externally (section 4), and we use the dynamic and thermodynamic perspectives outlined above to interpret the response of the HC (section 5). Finally, we briefly consider how heat transport owing to a wind-driven ocean circulation may affect our results (section 6) before summarizing our conclusions (section 7).

2. Simulation design

a. Model configuration

We conduct simulations of an idealized equinoctial HC using version 6.9.5 of the System for Atmospheric Modeling (SAM; Khairoutdinov and Randall 2003)

coupled to a two-stream semigray radiation parameterization. The model configuration is identical to that used in the gray radiation simulations described in SK16, except that we consider an energetically closed lower boundary condition rather than imposing a fixed distribution of SST. The lower boundary condition and radiation parameterization are described in more detail below.

The model solves the anelastic governing equations for the vector velocity, the mixing ratios of total precipitating water and total nonprecipitating water, and the liquid/ice water static energy. We use a simple one-moment parameterization of microphysics and a 1.5-order subgrid-scale turbulence scheme, but we do not employ an explicit boundary layer or convection parameterization. Surface fluxes are calculated using bulk aerodynamic formulas with transfer coefficients evaluated based on Monin–Obukhov similarity theory.

The simulations are run on an equatorial beta plane extending from 69°S to 69°N, with periodic boundary conditions in the zonal direction and free-slip solid walls at the northern and southern boundaries. Two model domains are considered: a wide-domain configuration, in which the width of the domain is 138° of longitude and large-scale eddies are permitted, and a narrow-domain configuration, in which the domain width is 9° of longitude and only mesoscale and convective-scale eddies are able to form (see Fig. 1 of SK16). Here we refer to disturbances with characteristic zonal length scales $\gtrsim$ 1000 km as large-scale eddies, while those with shorter length scales are referred to as mesoscale or convective-scale eddies.

Following SK16, we use the diabatic acceleration and rescaling (DARE) technique of Kuang et al. (2005) in order to allow for the explicit simulation of moist convection at reasonable computational cost.[1] The DARE technique involves altering physical parameters in order to reduce the scale separation between convection and the large-scale flow. Specifically, the rotation rate of Earth is increased by a factor γ, while the radius of Earth and the time scales of all diabatic processes are reduced by the same factor. Together, these alterations reduce the size of the model domain required, but they do not alter important parameters of the large-scale flow, such as the ratio of the Rossby radius to Earth's radius. Further details of the DARE technique and an evaluation of its applicability to simulations of the HC are given in SK16.

The simulations are run with a horizontal grid spacing of 4 km, with the rotation rate, Earth radius, and diabatic time scales altered by the factor $\gamma = 10$, as described above. When the model domain is rescaled to the length and time scales appropriate for Earth's atmosphere, the effective horizontal grid spacing for large-scale hydrostatic flows is 40 km. All results shown here will be rescaled to the dimensions appropriate for Earth. The simulations use 46 vertical levels, with a vertical grid spacing increasing from 100 m near the surface to 1 km at the model top, which is set to 26.9 km. A sponge layer in the upper 30% of the domain relaxes the wind fields to their zonal-mean values to prevent gravity wave reflection. All simulations are run for 500 days, with 6-hourly snapshots over the last 200 days used to calculate time-mean fields in the analysis to follow.

b. Radiation scheme

We employ a *two-stream semigray radiation parameterization* closely following that described in O'Gorman and Schneider (2008). Solar insolation at the top of the atmosphere is prescribed as a time-independent function of latitude corresponding to perpetual equinox conditions with no diurnal cycle. The shortwave optical depth is specified as a function of pressure, and the surface shortwave albedo is set to 0.38 at all latitudes. The longwave optical depth is specified as a function of latitude and pressure with a maximum value at the equator. While this equatorial maximum crudely represents the strong greenhouse effect of water vapor in the tropics, neither the longwave optical depth nor the shortwave optical depth explicitly depend on the water vapor concentration or cloud amount. This allows for easier interpretation of the results without the interference of radiative feedbacks from water vapor and clouds. Full details of the functional forms used in the definitions of the longwave and shortwave optical depth and the solar insolation may be found in O'Gorman and Schneider (2008)[2]; our simulations use identical parameters to the "reference case" given in that paper.

c. Lower boundary condition

The lower boundary in our simulations is a mixed-layer ocean with a temperature T_s that varies only horizontally and evolves according to

$$C_o \frac{\partial T_s}{\partial t} = F_s + Q_o + K_o \nabla^2 T_s, \tag{1}$$

[1] The DARE technique is mathematically equivalent to the hypohydrostatic rescaling outlined in Pauluis et al. (2006) and Garner et al. (2007).

[2] O'Gorman and Schneider (2008) express optical depths in terms of their model's sigma coordinate, whereas in our anelastic simulations we use the base-state pressure.

where C_o is the heat capacity of the mixed layer, F_s is the net downward turbulent and radiative heat flux through the surface, Q_o represents the effect of horizontal ocean heat transport (OHT), and the last term on the right-hand side represents horizontal diffusion of the ocean temperature[3] with diffusion coefficient $K_o = 5000\,\mathrm{m^2\,s^{-1}}$. We take the mixed layer to have a depth of 2 m ($C_o = 8.3 \times 10^6\,\mathrm{J\,m^{-2}\,K^{-1}}$); tests using a deeper mixed layer (10 m) in the narrow-domain configuration indicate that the results are not sensitive to this choice. The effect of OHT will be discussed in section 6, where we describe a simple parameterization of low-latitude heat transport by the wind-driven ocean circulation. In sections 3–5, OHT is neglected, and we consider slab-ocean simulations in which Q_o is set to zero.

For comparison, we will also show some results from the gray radiation fixed-SST simulations described in SK16. These simulations are identical to the slab-ocean simulations outlined above, except they are run for only 250 days, and the SST distribution is specified as a function of latitude ϕ according to

$$T_s = T_{s0} - \delta T \sin^2(\phi), \tag{2}$$

where $T_{s0} = 300\,\mathrm{K}$ and δT is varied in the range 10–100 K.

3. Comparison of wide-domain and narrow-domain simulations

Figures 1a and 1b show the zonal-mean temperature and zonal-mean zonal wind in the wide- and narrow-domain slab-ocean simulations. In both cases, the deep tropics (equatorward of ~15°) are characterized by a relatively flat temperature distribution and weak easterly winds. Farther poleward, the magnitude of the meridional temperature gradient becomes larger, and the winds become increasingly westerly, culminating in a strong subtropical jet. In the wide-domain simulation, there is some evidence of an eddy-driven jet at midlatitudes, with westerly winds at the surface and aloft. The narrow-domain simulation also has an additional jet at midlatitudes, but this jet has almost no barotropic component, and the narrow-domain simulation is characterized by weak surface winds at all latitudes.

As a result of the lack of large-scale eddies in the narrow-domain case, there are large differences in eddy activity between the wide- and narrow-domain simulations (see also SK16). The wide-domain simulation exhibits a peak in eddy activity at midlatitudes; in the middle to upper troposphere there is a large convergence of the eddy momentum flux and a large maximum in eddy kinetic energy (Fig. 1c), and in the lower troposphere there is a strong poleward eddy heat flux (Fig. 1e). Here, the meridional eddy momentum flux is given by $\overline{u'v'}$, and the meridional eddy heat flux is given by $\overline{v'h'}$, where u and v are the zonal and meridional velocities, respectively, h is the moist static energy, the overbar represents a zonal and time mean, and the primes represent deviations from this mean. The moist static energy is defined as $h = c_pT + \Phi + L_vq$, where c_p is the specific heat capacity at constant pressure, T is the temperature, Φ is the geopotential, L_v is the latent heat of vaporization, and q is the water vapor mixing ratio. In the narrow-domain simulation, the eddy kinetic energy is relatively low, and the magnitudes of the meridional eddy fluxes of heat and momentum are several times smaller than in the wide-domain case (Figs. 1d,f).

The meridional overturning circulation also differs substantially between the wide- and narrow-domain simulations. Figures 2a and 2b show the streamfunction $\Psi = -\int_0^z \rho_0 \overline{v}\, dz'$ and angular momentum M in both cases. Here, $\rho_0(z)$ is the reference density used in the anelastic approximation dependent only on height z, and we follow SK16 in defining the angular momentum in our beta-plane simulations as $M = \overline{u} - fy/2$, where f is the Coriolis parameter, and y is the meridional distance from the equator. This definition ensures that M is conserved following the zonal-mean flow in the absence of eddies and frictional effects (SK16). The degree to which streamlines cross contours of M in the free troposphere therefore reflects the degree to which eddies influence the angular-momentum budget.

In the wide-domain case, a strong HC extends to roughly 20° of latitude in each hemisphere, with a weaker Ferrel cell existing on its poleward flank (Fig. 2a). Streamlines cross angular-momentum contours in both the Hadley and Ferrel cells, indicating the importance of momentum transport by baroclinic eddies for the global angular-momentum budget. In the narrow-domain simulation, the overturning circulation is much weaker; the HC is roughly one-third as strong as in the wide-domain case, and the Ferrel cell is completely absent (Fig. 2b). Here, and for the remainder of this paper, we define the HC strength to be the maximum magnitude of the hemispherically symmetrized

[3] Diffusion of T_s is included to eliminate gridpoint noise in the surface temperature field that develops in its absence. Similar gridpoint noise was found by Satoh (1994) in the surface temperature of axisymmetric GCM simulations of the HC with no convection parameterization. In our simulations, the HC is similar with or without diffusion applied to T_s, but the fields are smoother when diffusion is included, and for this reason we include diffusion in all the simulations shown.

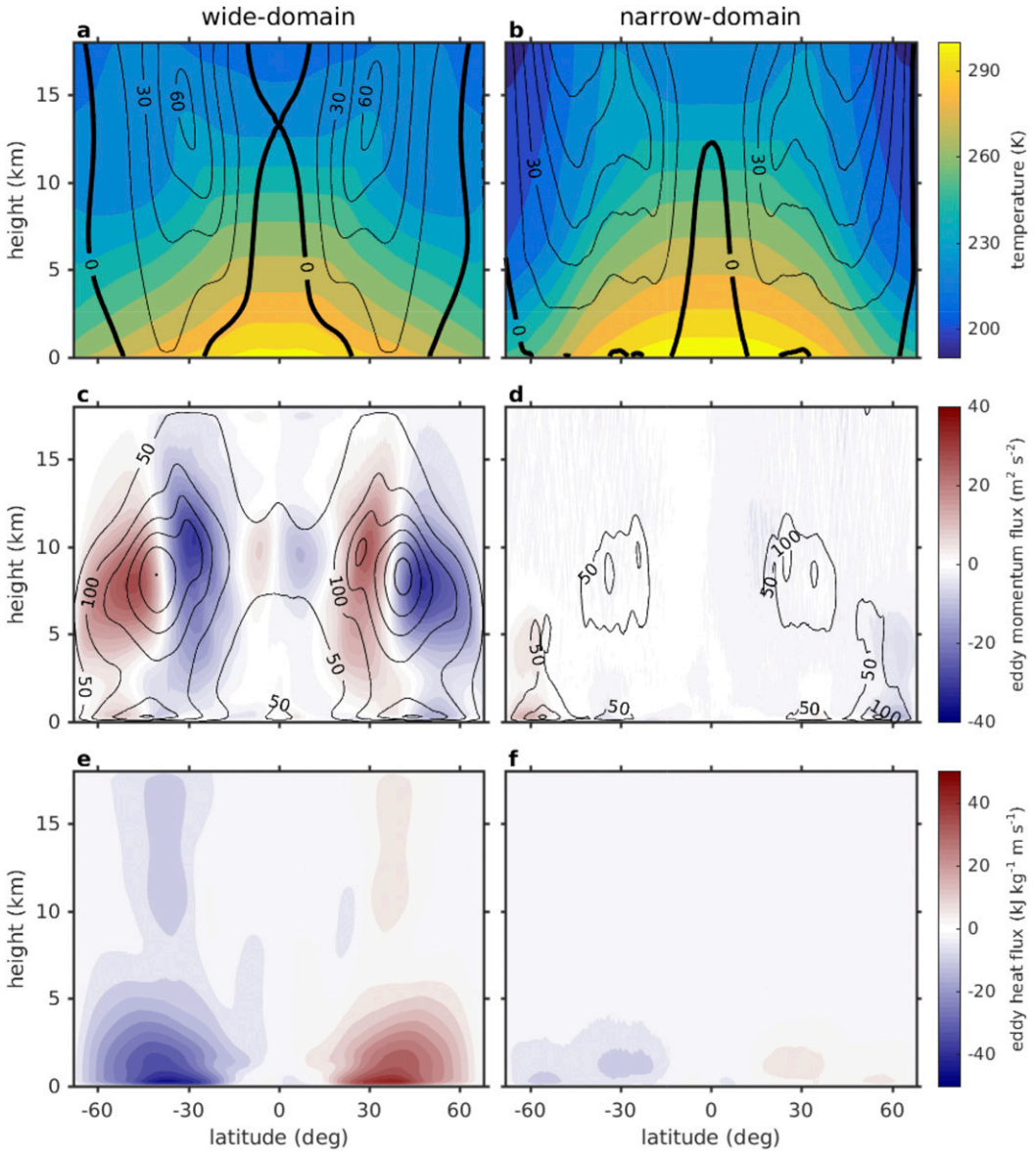

FIG. 1. Zonal- and time-mean properties of (left) wide-domain and (right) narrow-domain slab-ocean simulations. (a),(b) Temperature (colors) and zonal wind (contours; dashed negative; zero contour is thick; m s^{-1}). (c),(d) Meridional eddy momentum flux per unit mass $\overline{u'v'}$ (colors) and eddy kinetic energy per unit mass $\overline{u'^2} + \overline{v'^2}$ (contours; m^2 s^{-2}). (e),(f) Meridional eddy heat flux per unit mass $\overline{v'h'}$.

streamfunction. The weak overturning circulation in the narrow-domain simulation allows some crossing of streamlines and angular-momentum contours even though the eddy momentum fluxes are also relatively weak in this case.

The circulation in the wide-domain simulation exhibits broad similarities to Earth's annual-mean circulation, but there are some important differences, and these differences should be kept in mind when considering the potential implications of this work. For example, the beta-plane geometry used here gives rise to a biased distribution of eddy momentum fluxes, with a larger proportion of the eddy momentum flux shifted to the poleward side of the midlatitude jet. As a result, the vertically integrated eddy momentum flux at 30°S is ~70% as large in the wide-domain simulation as it is in the annual-mean of the NCEP–NCAR reanalysis (Kalnay et al. 1996). Furthermore, the eddy-driven jet in the wide-domain simulation is located equatorward of its position in the Southern Hemisphere of Earth's atmosphere; this may be partly related to the limited latitudinal extent of our domain. Finally, the HC in the

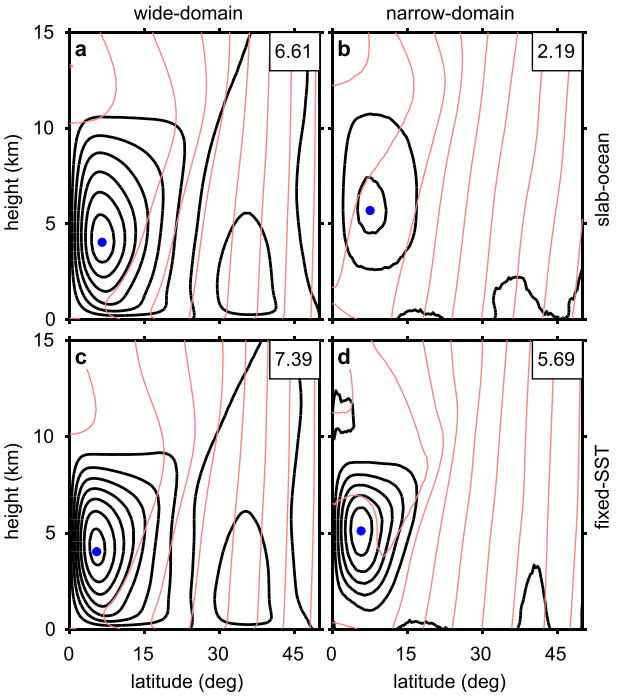

FIG. 2. Streamfunction (black; contour interval $10^3\,\mathrm{kg\,m^{-1}\,s^{-1}}$) and angular momentum M (red) in (a),(c) wide-domain and (b),(d) narrow-domain configurations. Simulations with (top) slab-ocean boundary condition and (bottom) SST specified according to (2) with $\delta T = 40$ K (see dashed line in Fig. 3). Angular-momentum contours are given for values corresponding to the angular momentum of the surface at latitudes of 0°, 6°, 12°, etc., and all data are symmetrized between hemispheres. Location of the hemispheric streamfunction extremum is marked with a blue dot, and HC strength ($10^3\,\mathrm{kg\,m^{-1}\,s^{-1}}$) is given in the top right of each panel.

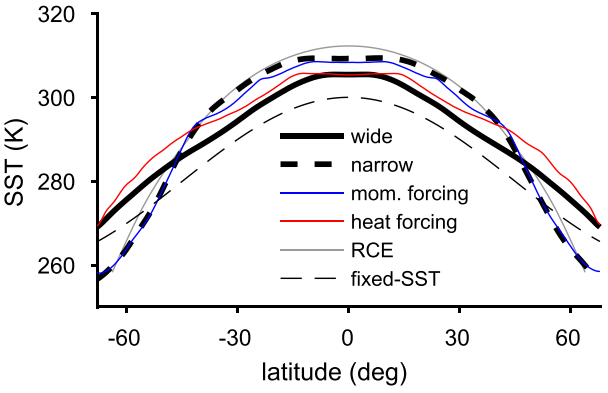

FIG. 3. Zonal- and time-mean SST in slab-ocean simulations. Wide-domain (thick solid black) and narrow-domain (thick dashed black) simulations, and simulations with applied momentum forcing (blue; $F_U = 1$) and applied heat forcing (red; $F_H = 1$). Gray line gives SST that would result if the atmosphere were in local RCE at each latitude, and thin dashed black line shows SST following (2) with $\delta T = 40$ K.

wide-domain simulation is substantially stronger than Earth's equinoctial HC [e.g., Levine and Schneider (2011) gives the strength of Earth's equinoctial HC in the Southern Hemisphere as $\sim 12 \times 10^{10}\,\mathrm{kg\,s^{-1}}$, equivalent to $3.0 \times 10^3\,\mathrm{kg\,m^{-1}\,s^{-1}}$ at 10° of latitude]. Levine and Schneider (2011) argued that a representation of low-latitude OHT is required to produce an HC in a regime similar to that of Earth's; we will consider simulations with a parameterization of OHT in section 6.

The strong sensitivity of the HC strength to domain width in the slab-ocean simulations contrasts with the fixed-SST results of SK16, where the HC strength was found to be similar in wide- and narrow-domain simulations with the same SST distribution. An example of a pair of such simulations is shown in Figs. 2c and 2d; despite the differences in the vertical structure of the circulations, the HC strength in each case is comparable. Furthermore, SK16 found that, as the pole-to-equator SST difference δT is increased, the HC strength increases in a similar fashion in both the wide- and narrow-domain configurations. The authors argued that, by specifying the SST distribution, a strong thermodynamic constraint is imposed on the flow, and this thermodynamic constraint acts independently of the eddy fluxes.

In the slab-ocean simulations, the steady-state SST distribution is determined by the energy budget of the mixed-layer ocean [see (1)], and this SST distribution differs considerably between the wide- and narrow-domain cases (Fig. 3). The narrow-domain SST has weak meridional gradients in the deep tropics (equatorward of ~15°) and very strong gradients in the midlatitudes and near the poleward edge of the domain. The wide-domain simulation, on the other hand, exhibits moderate meridional SST gradients in both the tropics and extratropics, except very close to the equator. Figure 3 also shows the SST that would arise if there were no large-scale meridional circulations and the atmosphere was in a state of radiative–convective equilibrium (RCE) at each latitude (gray line).[4] In the narrow-domain simulation, the meridional SST gradient near the equator is considerably weaker than this RCE surface temperature profile, indicating that the relatively flat SST distribution in the deep tropics of the narrow-domain simulation is a result of the circulation itself, rather than being an artifact of the radiative forcing.

[4] The RCE surface temperature profile is constructed using a series of small-domain simulations centered at different latitudes in the range 0°–64° and spaced 2° apart. Each simulation is conducted in a doubly periodic domain 16 × 16 grid points in size and run to equilibrium, with all other parameters identical to those of the slab-ocean simulations for the appropriate latitude.

The differences in SST distribution between the wide- and narrow-domain slab-ocean simulations provide some consistency between these slab-ocean results and the fixed-SST results of SK16. In both cases, a stronger meridional SST gradient in the deep tropics is associated with a stronger HC. The results are also consistent with the aquaplanet GCM simulations of Brayshaw et al. (2008), in which the HC strength was found to be sensitive to the subtropical SST gradient but less sensitive to changes in SST farther poleward. In our slab-ocean simulations, the SST is determined by the circulation itself, and the relationship between the SST gradient and HC strength is diagnostic rather than predictive. Nevertheless, the results highlight the potential utility of adopting a thermodynamic perspective in order to understand the tropical overturning circulation. Additionally, since large-scale eddy heat fluxes may have a strong influence on the meridional SST gradient in the slab-ocean simulations, the results suggest that such heat fluxes may play an important role in determining the strength of the HC.

4. Relative roles of eddy momentum fluxes and eddy heat fluxes

We evaluate the relative influence of large-scale eddy heat fluxes and large-scale eddy momentum fluxes on the simulated HC by conducting narrow-domain simulations in which the effects of large-scale eddies are specified externally. In particular, we conduct simulations with applied momentum forcing, in which a time- and longitudinally invariant forcing term, given by

$$\delta u_F = -F_U \frac{\partial}{\partial y}(\overline{u'v'})_{\text{wide}}, \tag{3}$$

is included as an additional tendency in the prognostic equation for the zonal wind. In (3), the term in parentheses on the right-hand side represents the meridional eddy momentum flux diagnosed from the wide-domain simulation, and F_U is a scalar that gives the magnitude of the applied momentum forcing. As before, the overbar represents a zonal and time mean, and the primes represent a deviation from this mean. To remove small-scale noise, the diagnosed eddy momentum flux is symmetrized between hemispheres and smoothed in latitude with a five-point moving-average filter prior to the calculation of the applied forcing. An identical method was used in SK16 to apply momentum forcing to fixed-SST simulations of the HC.

We also consider simulations with applied heat forcing, in which similar additional terms are included in the prognostic equations for the water vapor mixing ratio q and temperature[5] T:

$$\delta q_F = -F_H \frac{\partial}{\partial y}(\overline{v'q'})_{\text{wide}} \quad \text{and} \tag{4a}$$

$$\delta T_F = -F_H \frac{\partial}{\partial y}(\overline{v'T'})_{\text{wide}}. \tag{4b}$$

As for the momentum forcing, the terms in parentheses in (4) are diagnosed from the wide-domain simulation, symmetrized between hemispheres, and smoothed in latitude with a five-point moving-average filter. The scalar F_H gives the magnitude of the applied heat forcing.

The strength of the HC is increased when either heat forcing ($F_H = 1$) or momentum forcing ($F_U = 1$) is applied to the narrow-domain configuration (Figs. 4a,c). In the heat-forcing case, angular-momentum contours are displaced from the region of the HC, and the HC remains close to the angular-momentum-conserving limit. In the momentum-forcing simulation, on the other hand, the imposed forcing transports momentum from the subtropics and subpolar regions to the midlatitudes, allowing angular-momentum contours to cross streamlines in the descending branch of the HC. These differences in angular-momentum transport (along with differences in heat transport) between the heat-forcing and momentum-forcing simulations lead to substantially different distributions of temperature and zonal wind in each case (Figs. 4b,d).

The increase in HC strength is larger in the momentum-forcing ($F_U = 1$) simulation than in the heat-forcing ($F_H = 1$) case. In the momentum-forcing simulation, the HC strength is almost identical to that of the wide-domain simulation, and it is 3 times as strong as in the unforced narrow-domain simulation. In the heat-forcing simulation, the HC strength is increased by about 50% compared to the unforced narrow-domain simulation. These results indicate that, in contrast to the fixed-SST simulations shown in SK16, momentum transport by large-scale eddies plays a key role in determining the HC strength in simulations in which the surface temperature is interactive.

Applying both momentum forcing and heat forcing ($F_U = F_H = 1$; all forcing) to a simulation in the narrow-domain configuration roughly reproduces the circulation in the corresponding wide-domain case, although some differences do remain (Figs. 4e,f). For instance, in the all-forcing simulation, the subtropical jets extend to

[5] The prognostic thermodynamic variable in the model is the liquid/ice water static energy, but we show the forcing for temperature for simplicity. Eddy fluxes of condensed water are not included in the forcing fields.

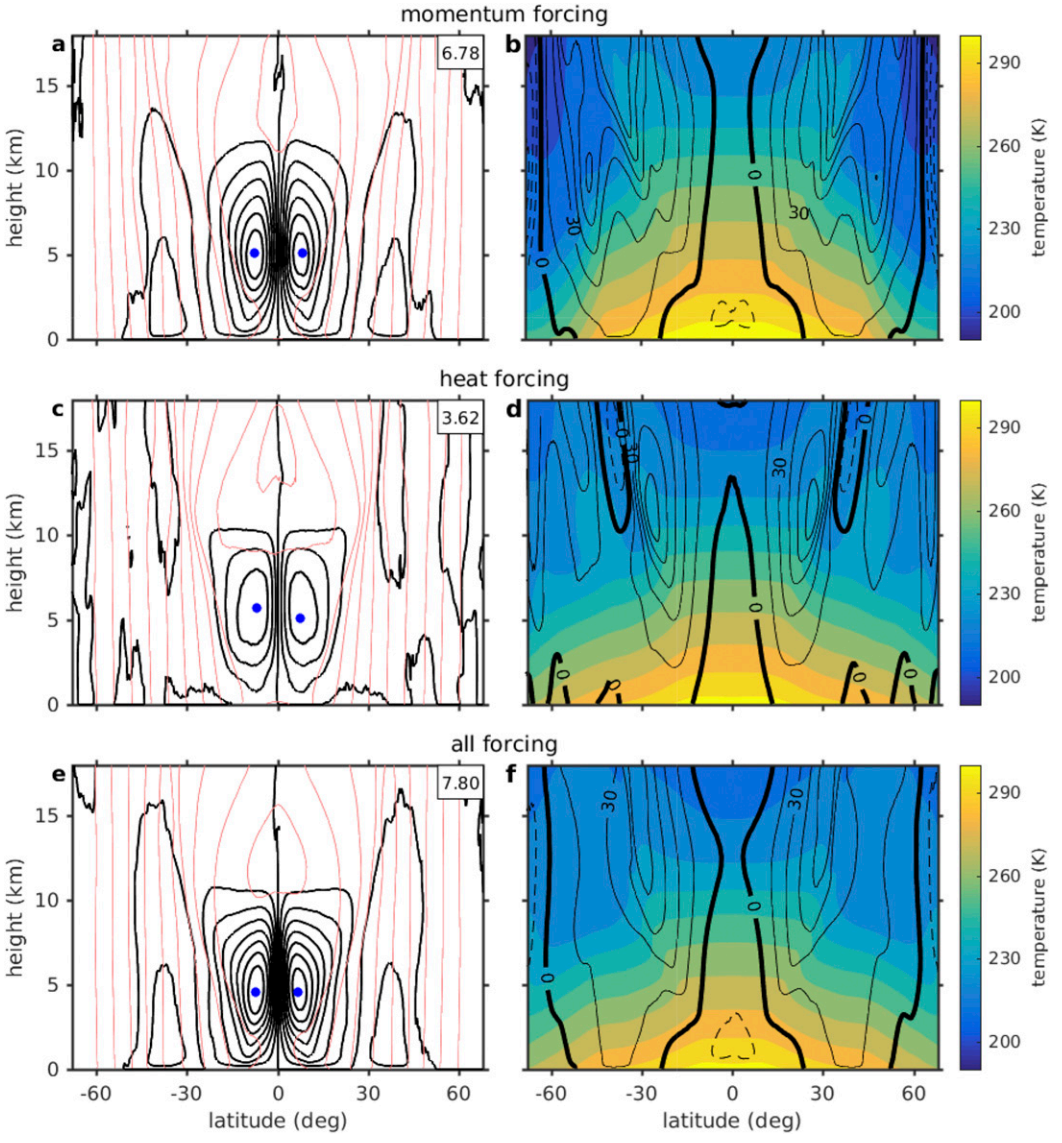

FIG. 4. (left) As in Fig. 2a, but showing both hemispheres and for narrow-domain simulations with applied (a) momentum forcing ($F_U = 1$), (c) heat forcing ($F_H = 1$), and (e) momentum and heat forcing ($F_U = F_H = 1$). (right) As in Fig. 1a, but for narrow-domain simulations with applied (b) momentum forcing ($F_U = 1$), (d) heat forcing ($F_H = 1$), and (f) momentum and heat forcing ($F_U = F_H = 1$).

lower altitudes, the meridional temperature gradient in the subtropics is larger, and the HC is somewhat stronger than in the unforced wide-domain case. These differences are partially a result of the neglect of vertical eddy transports in the applied forcing fields. In an alternative all-forcing simulation in which the applied forcing fields include horizontal eddy fluxes and large-scale (wavelength > 960 km) vertical eddy fluxes diagnosed from the wide-domain simulation, the HC strength is $7.2 \times 10^3\,\mathrm{kg\,m^{-1}\,s^{-1}}$, closer to its value in the wide-domain case. More fundamentally, however, the forced simulations do not include the feedback between the eddy fluxes and the mean flow, and this also contributes to the differences between the circulation in the all-forcing simulation and that of the wide-domain simulation. Nevertheless, the broad similarity between the results from the all-forcing simulation (Figs. 4e,f) and those of the wide-domain simulation (Figs. 1a, 2a) provides some confidence that the externally applied forcing is able to reproduce the effect of large-scale eddies on the zonal-mean flow to a reasonable degree. Furthermore, the increase in the HC strength between the all-forcing simulation and the unforced narrow-domain simulation ($\approx 5.6 \times 10^3\,\mathrm{kg\,m^{-1}\,s^{-1}}$) is similar

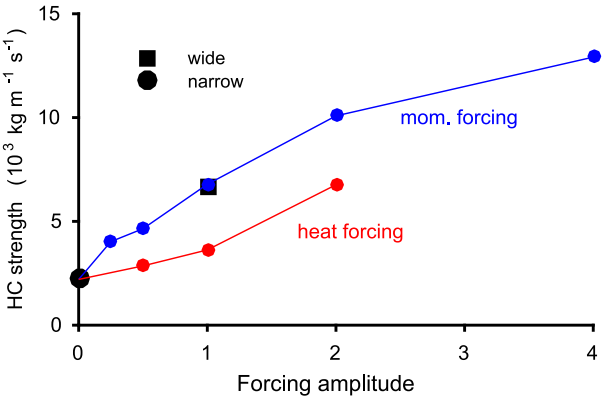

FIG. 5. HC strength as a function of forcing amplitude F_U or F_H in narrow-domain slab-ocean simulations with applied momentum forcing (blue) and applied heat forcing (red). Unforced narrow-domain simulation (black circle) and unforced wide-domain simulation (black square) are plotted at forcing amplitudes of zero and one, respectively.

to the sum of the increases resulting from momentum forcing and heat forcing alone ($\approx 5.9 \times 10^3\,\mathrm{kg\,m^{-1}\,s^{-1}}$). This indicates that our decomposition of large-scale eddy effects into those associated with momentum fluxes and those associated with heat fluxes is meaningful, at least when applied to the HC strength.

The sensitivity of the HC to eddy fluxes may be further explored by varying the parameters F_U and F_H. For both momentum forcing and heat forcing, the HC strength increases monotonically with increasing forcing amplitude, even for magnitudes of the applied forcing substantially greater than unity (Fig. 5).[6] In all cases, momentum forcing produces the stronger HC at a given forcing amplitude, confirming the dominant role of large-scale eddy momentum fluxes in influencing the HC strength at a wide range of forcing amplitudes. This contrasts with the results of Schneider (1984), who found a relatively weak dependence of the HC strength on the magnitude of a prescribed distribution of eddy momentum fluxes in two-dimensional simulations in which the convective heating was specified. In our simulations, the effects of convection are calculated interactively by the model, and the feedback due to convection likely alters the response. Nevertheless, it should be noted that our results are obtained for a particular eddy field as generated by the wide-domain simulation. A different eddy field may have different patterns of heat fluxes and momentum fluxes, and this would affect the response of the HC. For the case of linear Rossby waves, the relative magnitude of the eddy heat flux versus the eddy momentum flux is determined by the vertical and horizontal group velocities of the eddies (e.g., Edmon et al. 1980). These propagation characteristics depend on the circulation itself, and this feedback is neglected when the forcing amplitude is varied via the factors F_U and F_H without any modification to the spatial pattern of the forcing.

[6] We limit the heat forcing to $F_H \leq 2$ to avoid simulations with large SST minima in the subtropics.

5. Application of the dynamic and thermodynamic perspectives

The results of the previous two sections confirm the importance of large-scale eddy momentum fluxes for the HC in the slab-ocean simulations. But it remains unclear why the sensitivity of the HC strength to large-scale eddies differs in the fixed-SST simulations of SK16. To provide further insight, we now interpret the results through the dynamic and thermodynamic perspectives outlined at the beginning of this paper.

a. *Dynamic perspective*

We first apply the dynamic perspective; we focus on the constraints placed on the HC by the zonal momentum budget. Consider the steady-state equation for the zonal-mean zonal wind:

$$-\overline{v}(\overline{\zeta}+f)+\overline{w}\frac{\partial\overline{u}}{\partial z}=\sigma+\frac{1}{\rho_0}\frac{\partial\overline{\tau_x}}{\partial z}. \tag{5}$$

Here, (u, v, w) represent the velocities in the directions (x, y, z), ζ is the relative vorticity, f is the Coriolis parameter, τ_x represents the zonal frictional stress, and

$$\sigma=-\frac{\partial}{\partial y}(\overline{u'v'})-\frac{1}{\rho_0}\frac{\partial}{\partial z}(\rho_0\overline{u'w'})$$

is the eddy momentum flux convergence. Above the boundary layer, frictional torques are small and may be neglected in (5). Furthermore, if we consider the region near the latitude of the hemispheric streamfunction extremum ϕ_m the flow is quasi horizontal, and the vertical advection term $\overline{w}\partial_z\overline{u}$ may also be neglected. Equation (5) may thus be simplified to give

$$f\overline{v}(1-\mathrm{Ro}_L)\approx-\sigma,$$

where $\mathrm{Ro}_L=-\overline{\zeta}/f$ is the local Rossby number. Integrating the above equation with mass weighting from the height at which the streamfunction reaches its maximum absolute value z_m to the height of the tropopause z_t, we may define a suitably weighted bulk Rossby number Ro such that

$$\Psi_{\max}(1-\mathrm{Ro}) \approx \mathcal{S}/f. \tag{6}$$

Equation (6) relates the maximum magnitude of the streamfunction at a given latitude $\Psi_{\max}$ to the strength of the eddy momentum flux divergence in the upper troposphere, $\mathcal{S} = -\int_{z_m}^{z_t} \rho_0 \sigma \, dz$. In particular, (6) allows a decomposition of the streamfunction maximum into a component that may be directly related to the eddy momentum fluxes $(1-\mathrm{Ro})\Psi_{\max}$ and a component that may be related to the mean flux of momentum $\mathrm{Ro}\Psi_{\max}$ (see also Schneider and Bordoni 2008). The bulk Rossby number is therefore a measure of the relative importance of mean momentum fluxes and eddy momentum fluxes in the subtropical momentum budget.

In the momentum-forcing simulations, the right-hand side of (6) must also include an external momentum source so that

$$\Psi_{\max}(1-\mathrm{Ro}) \approx \frac{\mathcal{S}+\mathcal{F}}{f}, \tag{7}$$

where

$$\mathcal{F} = -\int_{z_m}^{z_t} \rho_0 \delta u_{\mathcal{F}} \, dz.$$

The predictive value of (7) depends on the behavior of the bulk Rossby number Ro. If $\mathrm{Ro} \ll 1$, changes in the eddy momentum flux divergence and/or the applied momentum forcing must be balanced by changes in the streamfunction maximum. If the latitude ϕ_m remains roughly constant, this implies a linear relationship between the HC strength and the magnitude of the eddy momentum forcing $\mathcal{S}+\mathcal{F}$ (Walker and Schneider 2006). However, for values of Ro of order unity, the relationship between $\mathcal{S}+\mathcal{F}$ and the HC strength may be more complex.

Figure 6 shows $\Psi_{\max}$ plotted against the right-hand side of (7) for both the unforced and forced simulations. Following SK16, we evaluate these quantities at 10° of latitude rather than at ϕ_m. While the approximations used to derive (7) are best satisfied at ϕ_m, the bulk Rossby number in the momentum-forcing simulations is not well defined at this location because it is close to the latitude at which the applied momentum tendencies change sign. Nevertheless, the ratio of $(\mathcal{S}+\mathcal{F})/f$ and $\Psi_{\max}$ in Fig. 6 may be taken as an estimate of $1-\mathrm{Ro}$ at 10° of latitude.

The bulk Rossby number in the wide-domain simulation and the momentum-forcing simulations is lower than in the narrow-domain simulations with no forcing or with heat forcing alone. In the momentum-forcing simulations, the streamfunction maximum increases along with $(\mathcal{S}+\mathcal{F})/f$, qualitatively consistent with the behavior of the dynamical constraint (7) at fixed bulk Rossby number Ro. But even for strong momentum forcing, the value of Ro remains relatively high ($\mathrm{Ro} > 0.6$ for $F_U \leq 2$), and variations in Ro must be taken into account in order to quantitatively connect the eddy momentum forcing $\mathcal{S}+\mathcal{F}$ to the strength of the circulation as measured by $\Psi_{\max}$. In the heat-forcing simulations, $\Psi_{\max}$ increases despite a lack of increase in the eddy momentum forcing $\mathcal{S}+\mathcal{F}$, Ro remains close to unity, and (7) provides little insight into the strength of the HC.

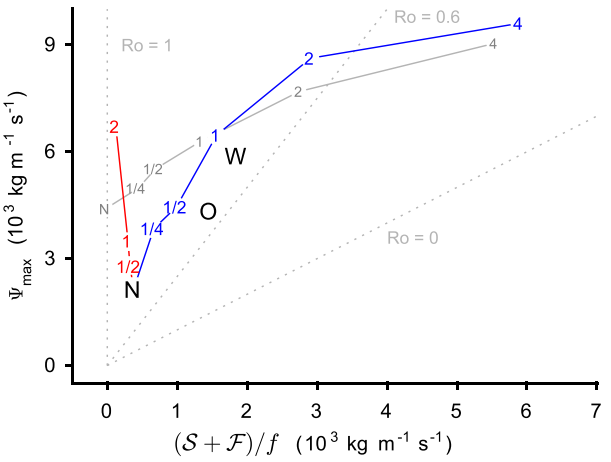

FIG. 6. Streamfunction maximum $\Psi_{\max}$ plotted against $(\mathcal{S}+\mathcal{F})/f$, both evaluated at 10° of latitude. Numbers give the forcing magnitude (F_U or F_H) in slab-ocean simulations with applied momentum forcing (blue) and heat forcing (red) and in fixed-SST simulations with applied momentum forcing (gray; δT = 40 K). Letters give results for unforced wide-domain simulations with slab-ocean (W) and parameterized OHT (O), and unforced narrow-domain simulations (N) with slab ocean (black) and fixed SST (gray; δT = 40 K). The tropopause height z_t is taken to be 15 km, and flow statistics are calculated based on fields symmetrized between hemispheres. Gray dotted lines give contours of bulk Rossby number (Ro) at the values shown.

Variations in Rossby number are also associated with the differing responses of the circulation strength to momentum forcing in the slab-ocean simulations compared to in the fixed-SST case of SK16. The gray solid line in Fig. 6 shows results from fixed-SST narrow-domain simulations with δT = 40 K and with momentum forcing of varying amplitudes in the range F_U = 0–4. Here, the momentum forcing is derived from a wide-domain simulation with an identical SST distribution (δT = 40 K). While the streamfunction maximum $\Psi_{\max}$ increases with increasing momentum-forcing amplitude in the fixed-SST simulations, the increase is weaker than in the slab-ocean case, particularly at low to moderate forcing amplitudes. These results suggest that, while the dynamic perspective embodied in (7) provides a conceptual basis for understanding how large-scale eddy

momentum fluxes contribute to a strengthening of the HC, a theory for the bulk Rossby number Ro is required to use this perspective for quantitative prediction in the large Rossby number regime. We do not attempt to construct such a theory here. Instead, we consider the insights that may be gained from an alternative thermodynamic perspective of the HC.

b. Thermodynamic perspective

The results from the unforced simulations in section 3 suggest that the meridional gradient of SST in the deep tropics (equatorward of ~15°) may be a useful diagnostic for understanding the HC strength. In the forced simulations, however, the relationship between this SST gradient and the HC strength is less clear (Fig. 3). For instance, the HC strength is almost identical in the momentum-forcing ($F_U = 1$) and wide-domain simulations despite the fact that the near-equatorial SST gradient is substantially larger in the wide-domain case.

A more physically based diagnostic may be constructed by considering the distribution of entropy in the tropical boundary layer. The boundary layer entropy is closely related to the SST, but it also depends on the near-surface humidity. According to the convective quasi-equilibrium theory of Emanuel (1995), a thermally direct circulation in the tropics is required to exist if the meridional gradient of boundary layer entropy exceeds a critical value that may be expressed as

$$\frac{\partial s_c}{\partial y} = -\frac{f^2 y}{2\Delta T}, \tag{8}$$

where s_c is the critical entropy distribution and ΔT is the difference between the temperature in the boundary layer and at the tropopause.[7] Emanuel (1995) showed that, in the limit of vanishing absolute vorticity (i.e., $\mathrm{Ro}_L = 1$) at the tropopause, a supercritical gradient of boundary layer entropy leads to a thermally direct circulation with an associated balanced surface zonal wind given by

$$u_s = \frac{\Delta T}{f}\frac{\partial (s_b - s_c)}{\partial y}. \tag{9}$$

Here, s_b is the entropy distribution in the boundary layer, which is taken to be

$$s_b = c_p \log(\overline{T_b}) - R_d \log\left(\frac{\overline{p_b}}{p_0}\right) + \frac{L_v \overline{q_b}}{T_0}, \tag{10}$$

where T_b, p_b, and q_b are the temperature, pressure, and water vapor mixing ratio, respectively, all evaluated at the lowest model level and symmetrized between hemispheres, $T_0 = 273.15\,\mathrm{K}$, and $p_0 = 10^5\,\mathrm{Pa}$. Assuming an Ekman-induced meridional flow in the boundary layer, (9) suggests that the strength of the meridional circulation depends on the degree to which gradients in s_b exceed their critical value.

Equation (9) is derived under the assumptions that $\mathrm{Ro}_L = 1$ at the tropopause and that convective quasi equilibrium, which requires a fixed relationship between the boundary layer entropy s_b and the saturation entropy in the free troposphere s^* (Emanuel et al. 1994), holds throughout the HC.[8] In our simulations, however, Ro_L differs substantially from unity in the upper troposphere of the momentum-forcing and wide-domain simulations (see Fig. 6). Furthermore, in simulations with a strong HC, the midtropospheric value of $s^* - s_b$ is substantially greater near the HC edge compared to at the equator (Fig. 7), indicating that convective quasi equilibrium is violated in the HC descending branch. Indeed, for cases with the strongest HCs ($F_u \geq 2$) the precipitation rate is close to zero, and convection is almost entirely suppressed in the subtropics (~15°–30°) (not shown).

While the results above suggest that the convective quasi-equilibrium theory cannot be directly applied to our simulations, the critical entropy in (8) may nevertheless be relevant for the tropical circulation. For instance, consider the case where the assumption of convective quasi equilibrium is relaxed, and instead we simply require that the lapse rate be moist adiabatic in the free troposphere. Additionally, rather than assuming $\mathrm{Ro}_L = 1$ at the tropopause, we assume that the zonal wind in the boundary layer is weak relative to that of the upper troposphere. As pointed out by Emanuel (1995), (8) then becomes a condition on the saturation entropy of the free troposphere. In particular, with the two assumptions above, the right-hand side of (8) gives the strongest meridional gradient in free-tropospheric saturation entropy that may be maintained in an atmosphere that is in thermal wind balance and that is stable to inertial motions (i.e., $\mathrm{Ro}_L \leq 1$).

[7] Equation (8) is equivalent to (8) of Emanuel (1995) under the beta-plane approximation and assuming that the zonal winds at the equatorial tropopause are weak.

[8] If convection acts to return the atmosphere to a neutral state with respect to an undilute parcel ascent, the assumption of convective quasi equilibrium reduces to the requirement that the saturation entropy in the free troposphere is locally equal to the entropy within the boundary layer. But if entrainment into convective clouds is taken into account, the relevant neutral state corresponds to one in which the saturation entropy decreases with height (Singh and O'Gorman 2013), as is found at the equator in our simulations (Fig. 7).

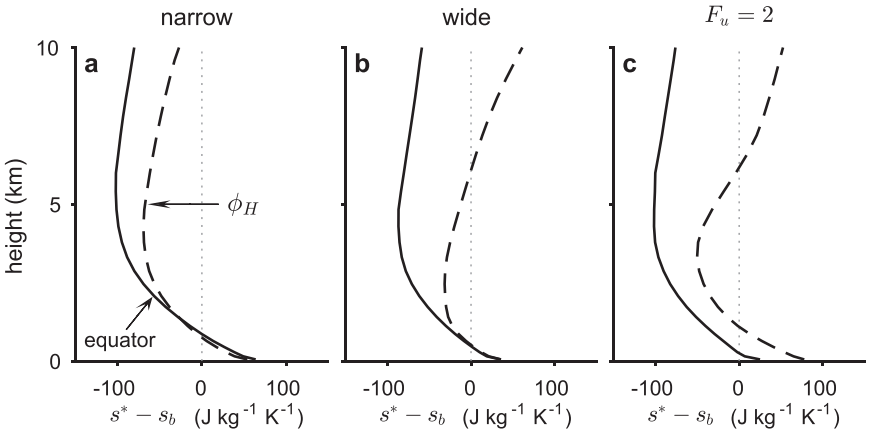

FIG. 7. Difference between saturation entropy s^* and entropy in the boundary layer s_b evaluated at the equator (solid) and at the HC edge as measured by the latitude ϕ_H (dashed) for unforced (a) narrow-domain and (b) wide-domain simulations, and (c) momentum-forcing simulation with $F_u = 2$. Saturation entropy is calculated using (10) but evaluated at all model levels and with the mixing ratio q replaced by the saturation mixing ratio.

In the simulations, the meridional variation in mid-tropospheric saturation entropy is similar to that of the critical entropy distribution equatorward of ~20°, even in cases where the bulk Rossby number Ro is not close to unity (Fig. 8 shows the wide-domain simulation as an example). Maintaining meridional gradients of s_b that are substantially supercritical therefore requires the violation of convective quasi equilibrium, and it implies the existence of a large-scale circulation. In particular, if we assume that convective quasi equilibrium is well satisfied at the equator, the degree to which the distribution of s_b is supercritical may be considered to be a measure of the strength of the subtropical inversion. Since the subtropical inversion is maintained by the large-scale subsidence associated with the descending branch of the HC, this suggests a possible relationship between the HC strength and the boundary layer entropy distribution. We therefore argue that the degree of supercriticality of the boundary layer entropy distribution may be a good diagnostic for the strength of the tropical overturning whether or not convective quasi equilibrium is well satisfied throughout the HC.

To test the above hypothesis, we define a supercriticality parameter, $(\Delta s_b - \Delta s_c)/c_p$, where Δs_b represents the difference between the maximum value of s_b and the value of s_b at the edge of the HC, and Δs_c is the equivalent measure for the critical entropy distribution (Fig. 8).[9] Here, we follow Shaw and Voigt (2016) and define the poleward edge of the HC (the latitude ϕ_H in Fig. 8) as the point at which the balanced zonal surface wind u_s switches from easterly to westerly as one moves poleward.[10] By (9), this is the location at which the entropy difference $s_b - s_c$ reaches a minimum. The latitude ϕ_H varies between 23° and 26° across the unforced and forced simulations, and it is generally within a few degrees of a measure of the edge of the HC based on the latitude at which the magnitude of $\Psi_{\max}$ is reduced to 20% of its hemispheric maximum value. To calculate s_c, we assume that the temperature difference between the boundary layer and the tropopause is fixed at $\Delta T = 80$ K. This is a reasonable approximation for the simulations, and it means that s_c has the same latitudinal dependence across all cases.

Figure 9 shows the HC strength plotted against the supercriticality parameter for the unforced and forced slab-ocean simulations. There is a strong linear relationship between these quantities, with a least squares fit explaining $R^2 = 93\%$ of the variance. In the slab-ocean simulations, the boundary layer entropy distribution is dependent on the circulation itself, and the relationship between the supercriticality and the HC strength cannot be used to establish causality. For example, an increase in the momentum-forcing amplitude F_U may cause both a stronger HC and a larger supercriticality, even though there is no direct relationship between the supercriticality and the HC. However, a

[9] Note that both s_b and s_c are only defined up to a constant, and their absolute values do not have any physical meaning.

[10] Other authors have suggested that the HC extends to the latitude at which baroclinic eddies are first able to reach the upper troposphere (Korty and Schneider 2008; Levine and Schneider 2015). However, such a definition cannot be relevant for the narrow-domain simulations, in which such eddies are absent.

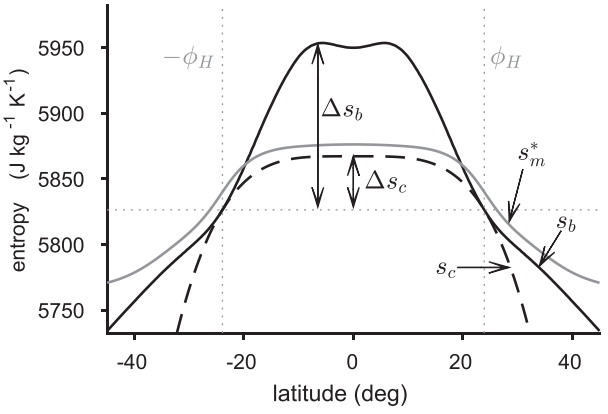

FIG. 8. Boundary layer entropy s_b (solid black) and midtropospheric saturation entropy s_m^* (solid gray) in wide-domain slab-ocean simulation, and critical entropy s_c (dashed black) plotted such that $s_b = s_c$ at latitude $\phi = \phi_H$. Double-headed arrows indicate the entropy deficit Δs_b and the critical entropy deficit Δs_c (see text). The value of s_m^* is calculated using (10) but evaluated at 7 km rather than at the lowest model level and with the mixing ratio q replaced by the saturation mixing ratio.

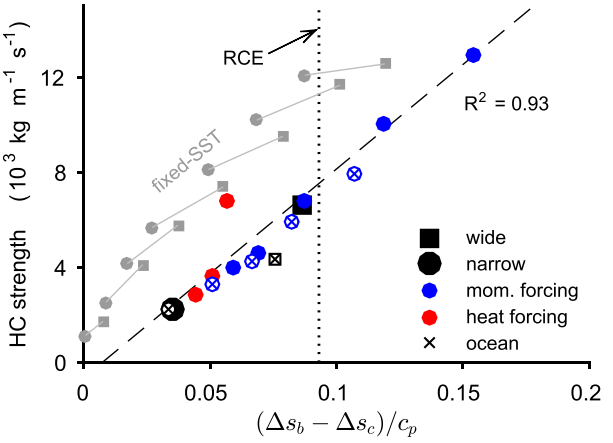

FIG. 9. HC strength plotted against supercriticality parameter $(\Delta s_b - \Delta s_c)/c_p$ in wide-domain (squares) and narrow-domain (circles) configurations. Interactive-SST simulations with applied momentum forcing (blue symbols), applied heat forcing (red symbols), and with no applied forcing (black symbols); solid symbols give slab-ocean results, and symbols with a cross give parameterized-OHT results. Fixed-SST simulations of SK16 with δT = 10, 20, 30, 40, 60, 80, and 100 K are shown in gray symbols, with lines connecting simulations with identical SST distributions. Vertical dotted line gives supercriticality for RCE solution (see section 3). Dashed line shows linear best fit to the slab-ocean simulations.

strong relationship between the supercriticality and the HC strength is also seen in the fixed-SST simulations of SK16 (gray symbols in Fig. 9).[11] When the SST is fixed, the ability of eddies to alter the boundary layer entropy distribution is reduced, and the direct influence of the boundary layer entropy distribution on the circulation may be diagnosed more readily. One caveat to this conclusion is that, even in the fixed-SST simulations, the circulation has some effect on the boundary layer entropy gradient through the advection of low-level moisture. For instance, for a given value of the pole-to-equator SST difference δT, both the supercriticality and the HC strength are larger in the wide-domain configuration compared to the narrow-domain case (Fig. 9), with the differences in supercriticality being primarily a result of differences in low-level humidity. Nevertheless, we argue that, taken together, the slab-ocean and fixed-SST results suggest that the supercriticality parameter is an important determinant of the HC strength.[12] Furthermore, the results support a thermodynamic view of the circulation in which the role of eddies is primarily effected through their influence on the boundary layer entropy distribution.

c. *The influence of large-scale eddies on the boundary layer entropy*

We now consider the mechanisms by which large-scale eddies may influence the boundary layer entropy s_b and the supercriticality. We focus on variations in s_b that are associated with vertically coherent variations in entropy and that are forced by eddy-induced variations in the meridional heat transport. While changes to the vertical profiles of temperature and humidity may also result in changes to the boundary layer entropy distribution, such effects are neglected in the qualitative discussion to follow.

In the wide-domain simulation, large-scale eddies transport heat from the subtropics (~15°–30°) to higher latitudes (Fig. 1e). The direct effect of these meridional eddy heat fluxes is to cool the subtropics relative to the equatorial region, thereby acting to increase the supercriticality. This is consistent with the increase in supercriticality (and HC strength) seen in the heat-forcing simulations as the forcing amplitude F_H is increased (Fig. 9). In addition to the direct effect, large-scale eddies influence the distribution of s_b indirectly through their effects on the mean meridional circulation. For instance, in the heat-forcing simulations, both

[11] The fixed-SST and slab-ocean simulations do not lie on the same line in Fig. 9. The reasons for this difference are currently being investigated.

[12] Note that the supercriticality in the RCE solution described in section 3 is larger than either the wide- or narrow-domain simulations with no forcing (Fig. 9). Based on the relationship in Fig. 9, this provides further evidence that the weak HC in the narrow-domain simulation is associated with transports of heat and moisture by the tropical circulation itself rather than weak gradients in the radiative forcing.

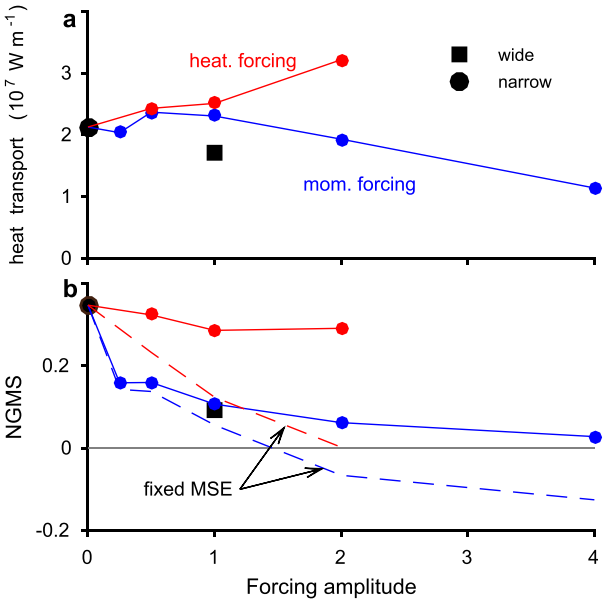

FIG. 10. (a) HC heat transport and (b) NGMS in slab-ocean simulations with applied momentum forcing (blue) and applied heat forcing (red) as a function of forcing amplitude (F_U or F_H). Dashed lines in (b) give an alternative calculation of the NGMS in which the moist static energy and humidity profiles in (11) are fixed to their values in the unforced narrow-domain simulation. Results for unforced narrow-domain (black circle) and wide-domain (black square) simulations are shown at forcing amplitudes of zero and one, respectively.

the HC strength and the poleward heat transport associated with the HC increase with increasing forcing amplitude F_H (Fig. 10a). Here, we define the HC heat transport to be the meridional transport of heat owing to the mean circulation,

$$\langle \overline{v}\,\overline{h} \rangle = \int_0^\infty \rho_0 \overline{v}\,\overline{h}\, dz,$$

symmetrized between hemispheres and evaluated at the latitude of the hemispheric streamfunction extremum ϕ_m. (For convenience we take ϕ_m to be in the Northern Hemisphere in the following.) In the slab-ocean simulations, the HC transports heat from equatorial latitudes to the subtropics. An increase in this heat transport associated with a strengthening of the HC would therefore tend to reduce the supercriticality. According to the relationship in Fig. 9, this corresponds to a negative feedback between the HC strength and the supercriticality, and this feedback limits the increase in HC strength that may be achieved by the direct effect of large-scale eddy heat fluxes described above.

Momentum forcing, in contrast to heat forcing, does not have a direct effect on the boundary layer entropy distribution. However, the HC heat transport in the momentum-forcing simulations remains roughly constant or decreases as the forcing amplitude F_U increases, despite a corresponding large increase in HC strength (Fig. 10a). This suggests that momentum forcing influences the meridional heat transport in the atmosphere by reducing the efficiency with which the HC transports heat poleward. A quantitative measure of this efficiency is the normalized gross moist stability (NGMS), defined here as the ratio between the mean poleward heat transport and the mean equatorward latent heat transport,

$$\mathrm{NGMS} = -\frac{\langle \overline{v}\,\overline{h} \rangle}{L_v \langle \overline{v}\,\overline{q} \rangle}, \tag{11}$$

symmetrized between hemispheres and evaluated at ϕ_m. In the momentum-forcing simulations, the NGMS decreases strongly with increasing forcing amplitude F_U (Fig. 10b), thus allowing for an increase in the supercriticality and HC strength without producing a poleward heat transport that is incompatible with the energy budget. A reduction in NGMS also reduces the strength of the negative feedback between the HC strength and supercriticality that is implied by the relationship in Fig. 9. This allows for a larger increase in HC strength in response to momentum forcing than if the NGMS were higher. In the heat-forcing simulations, the NGMS remains relatively large as the heat-forcing amplitude F_H increases (Fig. 10b), and increases in heat forcing are accompanied by relatively modest increases in HC strength.

To understand how momentum forcing reduces the NGMS of the HC, we consider the vertical profile of meridional velocity at the latitude of the hemispheric streamfunction extremum ϕ_m. As the momentum-forcing magnitude F_U is increased, this velocity profile becomes increasingly surface intensified (Fig. 11a). Given that the corresponding moist static energy profiles have maxima at the surface (Figs. 11b,d), we would expect such a surface intensification of the HC mass flux to reduce the NGMS, provided the return flow does not occur at very high altitudes [see (11)]. Consistent with this expectation, the reduction in NGMS in the momentum-forcing simulations is primarily associated with variations in the meridional velocity rather than variations in the distributions of moist static energy or water vapor mixing ratio, at least for low to moderate forcing amplitudes (see blue dashed line in Fig. 10b). Furthermore, the wide-domain simulation also exhibits a surface-intensified HC mass flux, and it has a similar NGMS to the momentum-forcing simulation with $F_U = 1$. These results suggest that the surface intensification of the HC mass flux is an important contributor to the changes in NGMS seen in the momentum-forcing simulations. In

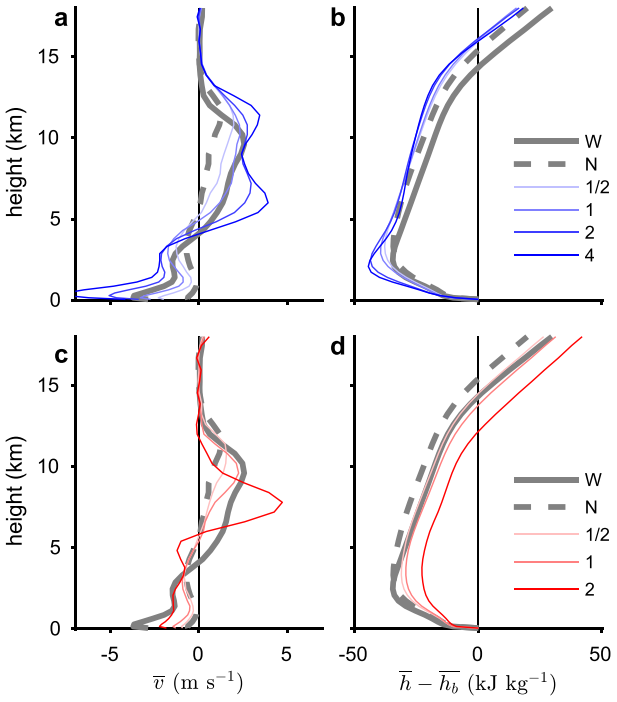

FIG. 11. Zonal- and time-mean profiles of (a),(c) meridional velocity and (b),(d) moist static energy symmetrized between hemispheres and plotted at the latitude of the Northern Hemispheric streamfunction extremum ϕ_m. Slab-ocean simulations with (top) applied momentum forcing and (bottom) applied heat forcing for forcing magnitudes F_U or F_H given in the legend. Unforced wide-domain (solid) and narrow-domain (dashed) simulations shown in gray. Moist static energy $\overline{h}$ is shown as difference from its value at the lowest model level $\overline{h_b}$.

the heat-forcing simulations, the meridional velocity profile at ϕ_m does not show a large intensification near the surface (Fig. 11c), and the NGMS remains roughly constant as the forcing amplitude F_H increases (Fig. 10b). However, in the heat-forcing case, both changes to the distributions of moist static energy and water vapor mixing ratio and changes to the meridional velocity profile at ϕ_m are important for the behavior of the NGMS as the forcing amplitude F_H increases (see red dashed line in Fig. 10b).

The differences in the strength of the low-level HC mass flux between the momentum-forcing and heat-forcing simulations may be understood by considering once more the steady-state equation for the zonal-mean zonal wind [see (5)]. Vertically integrating over the entire atmosphere with mass weighting gives

$$-\frac{\partial}{\partial y}\langle \overline{u}'\overline{v}'\rangle + \langle \delta u_F\rangle = \frac{\partial}{\partial y}\langle \overline{u}\,\overline{v}\rangle - \overline{\tau}_s, \qquad (12)$$

where τ_s is the frictional stress at the surface, and we have included the momentum-forcing term δu_F in the budget. The above equation expresses a balance between the convergence of the eddy momentum fluxes and the applied momentum forcing on the left-hand side, and the divergence of momentum owing to the mean flow and the sink of momentum owing to friction on the right-hand side. Outside the tropics, the divergence of the mean momentum flux may be neglected, and the forcing terms on the left-hand side of (12) can only be balanced by friction (e.g., Held 2000). For the HC in our simulations, however, the Rossby number Ro_L is not small, and mean momentum fluxes may be important. Nevertheless, the surface stress scales roughly with the left-hand side of (12) in the momentum-forcing simulations (not shown), implying that the low-level zonal wind increases with increasing forcing amplitude F_U. By Ekman balance, an increase in the low-level zonal wind is associated with an increase in the low-level meridional flow. The strong equatorward mass flux at low levels in the momentum-forcing simulations (Fig. 11a) may thus be explained as a frictional response to imposed torques in the upper troposphere.

The above argument is essentially the "downward control" principle outlined by Haynes et al. (1991); a divergence of momentum at upper levels results in a poleward meridional flow that must be closed within a frictional boundary layer near the surface. In the momentum-forcing simulations, this surface-intensified return flow results in a decrease in the NGMS of the HC and ultimately an increase in supercriticality as argued previously. For the heat-forcing case, the surface stress $\overline{\tau_s}$ is constrained to be small because of the lack of eddy momentum fluxes or applied momentum forcing on the left-hand side of (12). As a result, the near-surface meridional flow must remain relatively weak, even as the HC intensifies.

While the preceding discussion of the influence of eddies on the supercriticality is qualitative in nature, it nevertheless gives some insight as to the different mechanisms by which large-scale eddy fluxes of heat and momentum act to increase the HC strength. In particular, our analysis of the reduction in NGMS associated with the frictionally driven low-level flow in the momentum-forcing simulations provides a conceptual basis for understanding the influence of large-scale eddy momentum fluxes on the HC strength from a thermodynamic perspective. Further work is necessary to understand how changes in the vertical profiles of temperature and moisture may influence the boundary layer entropy and to explore the influences of large-scale eddies on the NGMS in more quantitative detail. Additionally, the arguments in this section have taken the relationship between the HC strength and the supercriticality as given. A greater understanding of the

dynamical mechanisms that give rise to this relationship is needed to determine the conditions under which such an assumption is warranted.

6. Wind-driven ocean circulation

In Earth's tropics, surface stresses associated with the low-level winds drive a meridional circulation in the ocean, comparable in mass flux to the HC, that is neglected in our slab-ocean simulations. The poleward heat transport owing to this wind-driven circulation plays an important role in the low-latitude energy budget (Held 2001; Trenberth and Caron 2001), and it potentially affects the dynamics of the HC (Levine and Schneider 2011). In this section, we apply a parameterization of low-latitude OHT to our simulations in order to investigate 1) how OHT affects the sensitivity of the HC strength to momentum forcing and 2) whether the relationship between the supercriticality and HC strength given in Fig. 9 still holds in simulations with a representation of OHT.

We consider a parameterization of low-latitude OHT following Levine and Schneider (2011) that is based on the simple model of the wind-driven subtropical overturning circulation outlined in Klinger and Marotzke (2000). Briefly, the ocean circulation is assumed to be composed of a single subtropical overturning cell in each hemisphere consisting of a poleward surface flow, a return flow along the thermocline, and an upwelling branch at the equator. The surface flow is given by the Ekman transport associated with the surface wind stress, and the interior return flow is assumed to be adiabatic. Under these conditions, the meridional heat transport associated with the ocean circulation F_o may be written as a function of the surface wind stress τ_s and the surface temperature distribution T_s (Klinger and Marotzke 2000) so that

$$F_o(y) = \int_{y_S}^{y} \left\{ c_o \frac{[\tau_s]}{f} \frac{\partial [T_s]}{\partial y'} - \delta(y')\Omega \right\} dy'. \qquad (13)$$

where c_o is the specific heat capacity of ocean water, and the square brackets signify a zonal mean (but not a time mean). The term multiplied by the Dirac delta function represents the upwelling at the equator, and it is given by

$$\Omega = \int_{y_S}^{y_N} c_o \frac{[\tau_s]}{f} \frac{\partial [T_s]}{\partial y''} dy''.$$

In the above equations, y_S and y_N denote the meridional extent of the cells and are defined as the most equatorward point at which $[\tau_s] = 0$ in the Southern and Northern Hemispheres, respectively. Outside of this latitude band, F_o is assumed to be zero. To prevent excessive upwelling-induced cooling at the equator, we follow Levine and Schneider (2011) and smooth the OHT convergence meridionally so that

$$Q_o = -\widetilde{\frac{\partial F_o}{\partial y}}, \qquad (14)$$

where the tilde represents a variable smoothed using a Gaussian filter with a standard deviation of 333 km. The OHT convergence Q_o is then added to the right-hand side of the equation governing T_s, (1), at each time step.

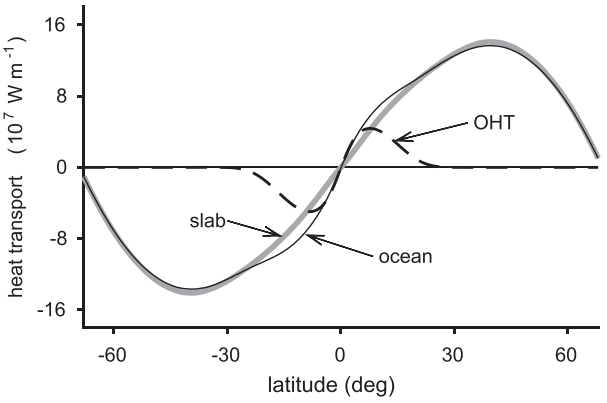

FIG. 12. Total meridional heat transport (ocean and atmosphere; solid black) and meridional OHT (dashed black) as a function of latitude for wide-domain simulation with parameterized OHT. Gray line shows total meridional heat transport in the corresponding slab-ocean simulation.

Simulations are conducted with the above OHT parameterization in the wide- and narrow-domain configurations and in the narrow-domain configuration with applied momentum forcing for amplitudes F_U in the range 0.25–2. For the momentum-forcing simulations, the forcing fields are derived from the wide-domain simulation that includes OHT. The resulting forcing fields are similar in both pattern and magnitude to the forcing fields used in the slab-ocean simulations.

Since the unforced narrow-domain simulation exhibits weak surface winds, it is almost unaffected by the inclusion of the OHT parameterization. In the wide-domain case, however, the OHT parameterization provides an additional poleward heat transport within the tropics that peaks at roughly 10° of latitude and extends to ~25° in both hemispheres (Fig. 12). The magnitude of this additional heat transport is substantial; in the deep tropics the parameterized OHT is comparable to the meridional heat transport associated with the HC in the corresponding slab-ocean simulation. Nevertheless, the total poleward heat transport (including heat transport owing to both the atmosphere and ocean) in

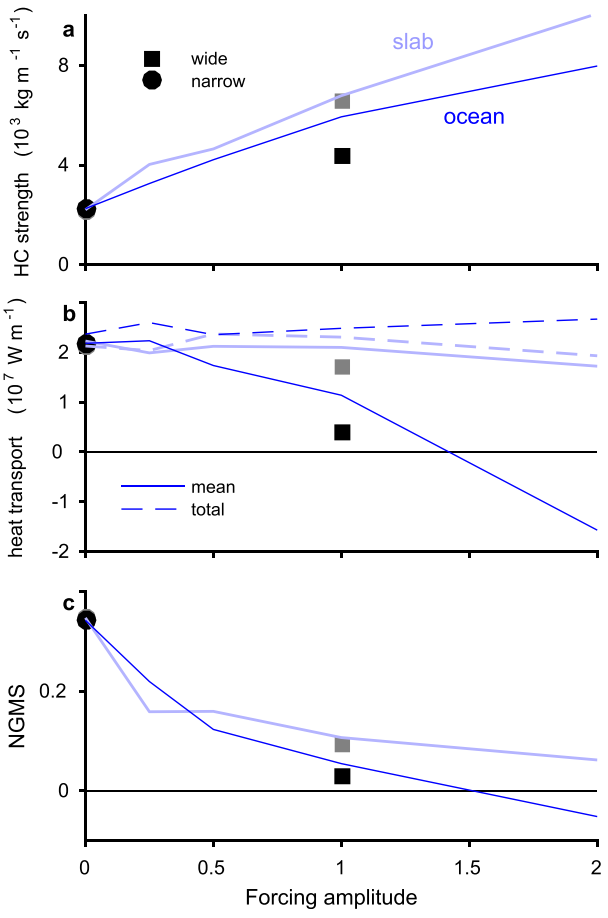

FIG. 13. (a) HC strength, (b) HC heat transport, and (c) NGMS in parameterized-OHT simulations (dark) and slab-ocean simulations (light). Results from narrow-domain simulations with applied momentum forcing (blue lines), unforced narrow-domain simulation (circles; plotted at a forcing amplitude of zero), and unforced wide-domain simulation (squares; plotted at a forcing amplitude of unity). Dashed lines in Fig. 13b show total poleward heat transport in momentum-forcing simulations symmetrized between hemispheres and evaluated at ϕ_m.

the wide-domain simulation increases only modestly when parameterized OHT is included because of a compensating reduction in the poleward heat transport associated with the HC (Fig. 13b). This reduction in the magnitude of the HC heat transport occurs primarily as a result of a reduction in NGMS (Fig. 13c) but also because of a weakening of the HC (Fig. 13a). In the parameterized-OHT simulations, the HC strength increases by only a factor of 2 between the narrow-domain and wide-domain cases (compared to a factor of 3 for the slab-ocean simulations), and the wide-domain HC strength is closer to that of Earth's equinoctial atmosphere when parameterized OHT is included than in the corresponding slab-ocean simulation. However, the bulk Rossby number remains relatively high (Ro $>$ 0.6; Fig. 6) with or without parameterized OHT (cf. Levine and Schneider 2011).

A similar compensation between the OHT and the HC heat transport is seen in the momentum-forcing simulations (blue lines in Fig. 13). In both the slab-ocean and parameterized-OHT cases, the HC strength increases with increasing momentum-forcing amplitude F_U, while the total poleward heat transport at the latitude ϕ_m remains roughly constant. In the slab-ocean simulations, this is because the HC heat transport also remains roughly constant as F_U is increased. But in the parameterized-OHT case, the magnitude of the OHT increases rapidly with F_U, and the HC heat transport decreases to compensate. For strong enough momentum forcing ($F_U = 2$), the HC heat transport changes direction, and the HC becomes a thermally indirect circulation with a negative NGMS.

Despite the large differences in the HC heat transport between the slab-ocean and parameterized-OHT simulations, the relationship between the HC strength and the supercriticality remains robust (Fig. 9). Furthermore, the HC strength responds similarly to increased momentum forcing with or without OHT (Fig. 13a), and in both cases the increase in HC strength is larger for applied momentum forcing ($F_U = 1$) than for applied heat forcing ($F_H = 1$) (not shown). These results confirm that the conclusions of the previous sections are not substantially altered by the inclusion of low-latitude OHT. At the same time, the strong variations in NGMS between the slab-ocean and parameterized-OHT simulations (in addition to the NGMS changes with momentum forcing outlined previously) highlight the difficulty in constructing a predictive theory for the HC heat transport or for the supercriticality. Understanding the factors that determine the degree of compensation between the OHT and the HC heat transport in response to eddy forcing would provide a step toward such a theory (cf. Kang et al. 2008, 2009).

7. Summary and conclusions

We have examined the role of large-scale eddies in determining the strength of the equinoctial Hadley circulation using idealized simulations conducted on an equatorial beta plane. In simulations with slab-ocean boundary conditions or with a simple parameterization of low-latitude ocean heat transport, the HC is found to be 2–3 times stronger in the presence of large-scale eddies (wide domain) compared to when such eddies are absent (narrow domain). These results are consistent with previous studies comparing the equinoctial HC in GCM simulations run in axisymmetric and three-dimensional configurations (Becker et al. 1997; Kim and Lee 2001; Walker and Schneider 2005).

We further investigated the relative influence of large-scale eddy momentum fluxes and large-scale eddy heat fluxes on the HC strength. Simulations in which the effects of large-scale eddies are prescribed externally reveal that both eddy heat fluxes and eddy momentum fluxes contribute to the amplification of the HC, but the effect of large-scale eddy momentum fluxes is found to be dominant. Walker and Schneider (2006) argued that the large influence of eddy momentum fluxes on the equinoctial HC is a result of a strong dynamical constraint placed on the flow by the angular-momentum budget in the limit of low Rossby number. In our simulations, however, the HC is in a regime where nonlinear advection of angular momentum by the mean flow is strong ($\mathrm{Ro} \gtrsim 0.6$), and this dynamical constraint is not sufficient to give a quantitative estimate of the HC strength. Moreover, the dynamical constraint gives little insight as to how eddy heat fluxes affect the HC or why the HC strength is relatively insensitive to large-scale eddy momentum fluxes in fixed-SST simulations, as found in SK16 and Satoh et al. (1995).

To reconcile our results with those of SK16, we considered a thermodynamic perspective of the HC motivated by the theory of Emanuel (1995). Consistent with this theory, a strong relationship is found to exist between the HC strength and a measure of the meridional entropy gradient in the tropical boundary layer in both the fixed- and interactive-SST cases. Based on these results, we hypothesize that an important pathway by which large-scale eddies influence the strength of the HC is through their effects on the boundary layer entropy. The weak influence of eddies on the HC strength in SK16 may then be explained as a result of the relative rigidity of the boundary layer entropy distribution when the SST is fixed.

In the interactive-SST simulations, large-scale eddies influence the boundary layer entropy distribution both directly and indirectly. The direct effect of meridional eddy heat fluxes is to cool the subtropical atmosphere, thereby increasing the magnitude of the meridional gradient of boundary layer entropy in the tropics. Large-scale eddy momentum fluxes, on the other hand, do not influence the boundary layer entropy directly, but they do so by altering the characteristics of the HC. In particular, meridional eddy momentum fluxes induce a low-level frictional component to the HC mass flux. Owing to the negative vertical gradient of moist static energy at low levels, this acts to reduce the efficiency with which the HC transports energy poleward, thereby also tending to increase the magnitude of the meridional gradient of boundary layer entropy. Such a mechanism is absent in previous studies of the HC using dry atmospheric models (e.g., Becker et al. 1997; Kim and Lee 2001), where a positive static stability implies that the (dry) static energy increases monotonically with height. Nevertheless, eddy-induced changes to the stratification may play a role in the response of the HC to large-scale eddies even in a dry atmosphere [see, e.g., Fig. 8 of Kim and Lee (2001)].

Given the relationship between the boundary layer entropy distribution and the HC strength found in our simulations, the thermodynamic perspective provides a qualitative framework for understanding the influence of large-scale eddy fluxes on the strength of the HC. To develop a fully predictive theory for the HC strength, however, the various influences on the boundary layer entropy must be quantified, and a quantitative theory for the NGMS must be constructed. As demonstrated by the differences in NGMS between the slab-ocean and parameterized-OHT simulations (including the appearance of negative NGMS in some cases), such a theory is far from trivial.

Further work is also required to determine the validity of the relationship between the HC strength and boundary layer entropy in more realistic configurations. Our simulations employ a simple semigray radiation scheme that neglects the influences of clouds and water vapor on the radiation field. When such influences are taken into account, the increased longwave cooling associated with a dry subtropical troposphere and the increased shortwave reflection associated with low-level subtropical clouds would both act to increase the supercriticality and potentially affect the HC strength. Our simulations also do not employ an explicit boundary layer turbulence parameterization, and this may affect the behavior of the simulated subtropical inversion. Analysis of the relationship between the boundary layer entropy gradient and the HC strength in simulations with comprehensive general circulation models is therefore a useful avenue for future work.

A further caveat to our study is that the simulated HC remains in a relatively large Rossby number regime, even when a representation of OHT is included in the simulations. Earth's equinoctial HC is closer to the linear regime, in which the dynamical constraint is stronger (Bordoni and Schneider 2008; Schneider and Bordoni 2008) and thermodynamic constraints may play a secondary role. On the other hand, the HC in our simulations lies in a similar Rossby number range as the cross-equatorial winter HC in Earth's atmosphere, and our results provide evidence that large-scale eddy momentum fluxes may be important for this cross-equatorial HC as well as for the equinoctial case (Caballero 2007, 2008). Furthermore, the potential role of large-scale eddy momentum fluxes in altering the NGMS of the HC may help to interpret changes to the HC heat transport

projected by climate model simulations of future global warming (e.g., Feldl and Bordoni 2016). Finally, while our simulations do not include zonal asymmetries and the associated stationary waves that are known to be important for the HC and monsoons (Caballero 2007; Shaw 2014), the thermodynamic perspective may nevertheless be useful for understanding the role of large-scale eddies in the onset of monsoons. Previous work has argued that eddy–mean flow feedbacks play a mediating role in the transition from the equinoctial to the solsticial HC through their effects on the momentum budget (Schneider and Bordoni 2008; Bordoni and Schneider 2008). Our results suggest that large-scale eddies could also play a role in influencing the timing and rapidity of monsoon onset through their effect on the energy budget, both directly, through their transports of heat, and indirectly, through their effect on the NGMS (see also Shaw 2014).

Acknowledgments. The authors thank M. Khairoutdinov for access to the SAM code and three anonymous reviewers for useful comments on an earlier version of this manuscript. Simulations used in this study were performed on the Harvard Odyssey cluster. This work was partially supported by NSF Grant AGS-1260380.

REFERENCES

Becker, E., G. Schmitz, and R. Geprägs, 1997: The feedback of midlatitude waves onto the Hadley cell in a simple general circulation model. *Tellus*, **49A**, 182–199, doi:10.1034/j.1600-0870.1997.t01-1-00003.x.

Bordoni, S., and T. Schneider, 2008: Monsoons as eddy-mediated regime transitions of the tropical overturning circulation. *Nat. Geosci.*, **1**, 515–519, doi:10.1038/ngeo248.

——, and ——, 2010: Regime transitions of steady and time-dependent Hadley circulations: Comparison of axisymmetric and eddy-permitting simulations. *J. Atmos. Sci.*, **67**, 1643–1654, doi:10.1175/2009JAS3294.1.

Brayshaw, D. J., B. Hoskins, and M. Blackburn, 2008: The storm-track response to idealized SST perturbations in an aqua-planet GCM. *J. Atmos. Sci.*, **65**, 2842–2860, doi:10.1175/2008JAS2657.1.

Caballero, R., 2007: Role of eddies in the interannual variability of Hadley cell strength. *Geophys. Res. Lett.*, **34**, L22705, doi:10.1029/2007GL030971.

——, 2008: Hadley cell bias in climate models linked to extra-tropical eddy stress. *Geophys. Res. Lett*, **35**, L18709, doi:10.1029/2008GL035084.

——, R. T. Pierrehumbert, and J. L. Mitchell, 2008: Axisymmetric, nearly inviscid circulations in non-condensing radiative-convective atmospheres. *Quart. J. Roy. Meteor. Soc.*, **134**, 1269–1285, doi:10.1002/qj.271.

Dickinson, R. E., 1971: Analytic model for zonal winds in the tropics. *Mon. Wea. Rev.*, **99**, 501–510, doi:10.1175/1520-0493(1971)099<0501:AMFZWI>2.3.CO;2.

Edmon, H. J., B. J. Hoskins, and M. E. McIntyre, 1980: Eliassen–Palm cross sections for the troposphere. *J. Atmos. Sci.*, **37**, 2600–2616, doi:10.1175/1520-0469(1980)037<2600:EPCSFT>2.0.CO;2.

Emanuel, K. A., 1995: On thermally direct circulations in moist atmospheres. *J. Atmos. Sci.*, **52**, 1529–1534, doi:10.1175/1520-0469(1995)052<1529:OTDCIM>2.0.CO;2.

——, J. D. Neelin, and C. S. Bretherton, 1994: On large-scale circulations in convecting atmospheres. *Quart. J. Roy. Meteor. Soc.*, **120**, 1111–1143, doi:10.1002/qj.49712051902.

Fang, M., and K. K. Tung, 1996: A simple model of nonlinear Hadley circulation with an ITCZ: Analytic and numerical solutions. *J. Atmos. Sci.*, **53**, 1241–1261, doi:10.1175/1520-0469(1996)053<1241:ASMONH>2.0.CO;2.

Feldl, N., and S. Bordoni, 2016: Characterizing the Hadley circulation response through regional climate feedbacks. *J. Climate*, **29**, 613–622, doi:10.1175/JCLI-D-15-0424.1.

Garner, S. T., D. M. W. Frierson, I. M. Held, O. Pauluis, and G. K. Vallis, 2007: Resolving convection in a global hypohydrostatic model. *J. Atmos. Sci.*, **64**, 2061–2075, doi:10.1175/JAS3929.1.

Haynes, P., M. McIntyre, T. Shepherd, C. Marks, and K. P. Shine, 1991: On the ''downward control'' of extratropical diabatic circulations by eddy-induced mean zonal forces. *J. Atmos. Sci.*, **48**, 651–678, doi:10.1175/1520-0469(1991)048<0651:OTCOED>2.0.CO;2.

Held, I. M., 2000: The general circulation of the atmosphere. *Proc. Geophysical Fluid Dynamics Program*, Woods Hole, MA, Woods Hole Oceanographic Institution, 54 pp. [Available online at https://www.whoi.edu/fileserver.do?id=21464&pt=10&p=17332.]

——, 2001: The partitioning of the poleward energy transport between the tropical ocean and atmospheres. *J. Atmos. Sci.*, **58**, 943–948, doi:10.1175/1520-0469(2001)058<0943:TPOTPE>2.0.CO;2.

——, and A. Y. Hou, 1980: Nonlinear axially symmetric circulations in a nearly inviscid atmosphere. *J. Atmos. Sci.*, **37**, 515–533, doi:10.1175/1520-0469(1980)037<0515:NASCIA>2.0.CO;2.

Kalnay, E., and Coauthors, 1996: The NCEP/NCAR 40-Year Reanalysis Project. *Bull. Amer. Meteor. Soc.*, **77**, 437–471, doi:10.1175/1520-0477(1996)077<0437:TNYRP>2.0.CO;2.

Kang, S. M., I. M. Held, D. M. W. Frierson, and M. Zhao, 2008: The response of the ITCZ to extratropical thermal forcing: Idealized slab-ocean experiments with a GCM. *J. Climate*, **21**, 3521–3532, doi:10.1175/2007JCLI2146.1.

——, D. M. W. Frierson, and I. M. Held, 2009: The tropical response to extratropical thermal forcing in an idealized GCM: The importance of radiative feedbacks and convective parameterization. *J. Atmos. Sci.*, **66**, 2812–2827, doi:10.1175/2009JAS2924.1.

Khairoutdinov, M. F., and D. A. Randall, 2003: Cloud resolving modeling of the ARM summer 1997 IOP: Model formulation, results, uncertainties, and sensitivities. *J. Atmos. Sci.*, **60**, 607–625, doi:10.1175/1520-0469(2003)060<0607:CRMOTA>2.0.CO;2.

Kim, H.-K., and S. Lee, 2001: Hadley cell dynamics in a primitive equation model. Part II: Nonaxisymmetric flow. *J. Atmos. Sci.*, **58**, 2859–2871, doi:10.1175/1520-0469(2001)058<2859:HCDIAP>2.0.CO;2.

Klinger, B. A., and J. Marotzke, 2000: Meridional heat transport by the subtropical cell. *J. Phys. Oceanogr.*, **30**, 696–705, doi:10.1175/1520-0485(2000)030<0696:MHTBTS>2.0.CO;2.

Korty, R. L., and T. Schneider, 2008: Extent of Hadley circulations in dry atmospheres. *Geophys. Res. Lett.*, **35**, L23803, doi:10.1029/2008GL035847.

Kuang, Z., P. N. Blossey, and C. S. Bretherton, 2005: A new approach for 3D cloud-resolving simulations of large-scale atmospheric circulation. *Geophys. Res. Lett*, **32**, L02809, doi:10.1029/2004GL021024.

Kuo, H., 1956: Forced and free meridional circulations in the atmosphere. *J. Meteor.*, **13**, 561–568, doi:10.1175/1520-0469(1956)013<0561:FAFMCI>2.0.CO;2.

Levine, X. J., and T. Schneider, 2011: Response of the Hadley circulation to climate change in an aquaplanet GCM coupled to a simple representation of ocean heat transport. *J. Atmos. Sci.*, **68**, 769–783, doi:10.1175/2010JAS3553.1.

——, and ——, 2015: Baroclinic eddies and the extent of the Hadley circulation: An idealized GCM study. *J. Atmos. Sci.*, **72**, 2744–2761, doi:10.1175/JAS-D-14-0152.1.

Lindzen, R. S., and A. Y. Hou, 1988: Hadley circulations for zonally averaged heating centered off the equator. *J. Atmos. Sci.*, **45**, 2416–2427, doi:10.1175/1520-0469(1988)045<2416:HCFZAH>2.0.CO;2.

O'Gorman, P. A., and T. Schneider, 2008: The hydrological cycle over a wide range of climates simulated with an idealized GCM. *J. Climate*, **21**, 3815–3832, doi:10.1175/2007JCLI2065.1.

Pauluis, O., D. M. W. Frierson, S. T. Garner, I. M. Held, and G. K. Vallis, 2006: The hypohydrostatic rescaling and its impacts on modeling of atmospheric convection. *Theor. Comput. Fluid Dyn.*, **20**, 485–499, doi:10.1007/s00162-006-0026-x.

Pfeffer, R. L., 1981: Wave–mean flow interactions in the atmosphere. *J. Atmos. Sci.*, **38**, 1340–1359, doi:10.1175/1520-0469(1981)038<1340:WMFIIT>2.0.CO;2.

Plumb, R. A., and A. Y. Hou, 1992: The response of a zonally symmetric atmosphere to subtropical thermal forcing: Threshold behavior. *J. Atmos. Sci.*, **49**, 1790–1799, doi:10.1175/1520-0469(1992)049<1790:TROAZS>2.0.CO;2.

Satoh, M., 1994: Hadley circulations in radiative–convective equilibrium in an axially symmetric atmosphere. *J. Atmos. Sci.*, **51**, 1947–1968, doi:10.1175/1520-0469(1994)051<1947:HCIREI>2.0.CO;2.

——, M. Shiobara, and M. Takahashi, 1995: Hadley circulations and their roles in the global angular momentum budget in two- and three-dimensional models. *Tellus*, **47A**, 548–560, doi:10.1034/j.1600-0870.1995.00104.x.

Schneider, E. K., 1977: Axially symmetric steady-state models of the basic state for instability and climate studies. Part II. Nonlinear calculations. *J. Atmos. Sci.*, **34**, 280–296, doi:10.1175/1520-0469(1977)034<0280:ASSSMO>2.0.CO;2.

——, 1984: Response of the annual and zonal mean winds and temperatures to variations in the heat and momentum sources. *J. Atmos. Sci.*, **41**, 1093–1115, doi:10.1175/1520-0469(1984)041<1093:ROTAAZ>2.0.CO;2.

Schneider, T., and S. Bordoni, 2008: Eddy-mediated regime transitions in the seasonal cycle of a Hadley circulation and implications for monsoon dynamics. *J. Atmos. Sci.*, **65**, 915–934, doi:10.1175/2007JAS2415.1.

Shaw, T. A., 2014: On the role of planetary-scale waves in the abrupt seasonal transition of the Northern Hemisphere general circulations. *J. Atmos. Sci.*, **71**, 1724–1746, doi:10.1175/JAS-D-13-0137.1.

——, and A. Voigt, 2016: What can moist thermodynamics tell us about circulation shifts in response to uniform warming? *Geophys. Res. Lett.*, **43**, 4566–4575, doi:10.1002/2016GL068712.

Singh, M. S., and P. A. O'Gorman, 2013: Influence of entrainment on the thermal stratification in simulations of radiative–convective equilibrium. *Geophys. Res. Lett.*, **40**, 4398–4403, doi:10.1002/grl.50796.

——, and Z. Kuang, 2016: Exploring the role of eddy momentum fluxes in determining the characteristics of the equinoctial Hadley circulation: Fixed-SST simulations. *J. Atmos. Sci.*, **73**, 2427–2444, doi:10.1175/JAS-D-15-0212.1.

Trenberth, K. E., and J. M. Caron, 2001: Estimates of meridional atmosphere and ocean heat transports. *J. Climate*, **14**, 3433–3443, doi:10.1175/1520-0442(2001)014<3433:EOMAAO>2.0.CO;2.

——, and D. P. Stepaniak, 2003: Seamless poleward atmospheric energy transports and implications for the Hadley circulation. *J. Climate*, **16**, 3706–3722, doi:10.1175/1520-0442(2003)016<3706:SPAETA>2.0.CO;2.

Walker, C. C., and T. Schneider, 2005: Response of idealized Hadley circulations to seasonally varying heating. *Geophys. Res. Lett.*, **32**, L06813, doi:10.1029/2004GL022304.

——, and ——, 2006: Eddy influences on Hadley circulations: Simulations with an idealized GCM. *J. Atmos. Sci.*, **63**, 3333–3350, doi:10.1175/JAS3821.1.

Williams, G. P., 1988a: The dynamical range of global circulations—I. *Climate Dyn.*, **2**, 205–260, doi:10.1007/BF01371320.

——, 1988b: The dynamical range of global circulations—II. *Climate Dyn.*, **3**, 45–84, doi:10.1007/BF01080901.